3-O-methyldopa in muscle. A microdialysis study. *Naunyn Schmiedeberg Arch Pharmacol* 1991;34:514–519.

27. Claustre J, Pequignot JM, Bui-xian B, Muchada R, Cottet-Emard RM, Peyrin L. Conjugation and deamination of circulating dopamine: relationship between sulfated and free dopamine in man. *J Auton Nerv Sys* 1990;29:175–182.

28. Frost JJ, Rosier AJ, Reich SG, et al. Positron emission tomographic imaging of the dopamine transporter with 11C-WIN 35428 reveals marked declines in mild Parkinson's disease. *Ann Neurol* 1993;34:423–431.

29. Volkow N, Ding YS, Fowler JS, et al. A new PET ligand for the dopamine transporter: studies in the human brain. *J Nucl Med* 1995;36:2252–2260.

30. VanderBorght TM, Kilbourn MR, Koeppe RA, et al. In vivo imaging of the brain vesicular monoamine transporter. *J Nucl Med* 1995;36:2162–2168.

31. Pate BD, Kawamata T, Yamada T, et al. Correlation of striatal fluoroDOPA uptake in the MPTP monkey with dopaminergic indices. *Ann Neurol* 1993;34:331–338.

32. Snow BJ, Tooyama I, McGeer EG, et al. Human positron emission tomographic

33. Firnau G, Chirakal R, Nahmias C, Garnett ES. Do the metabolites of [F18]fluoro-L-Dopa and [18F]fluoro-meta-tyrosine contribute to the accumulation of [F-18] in the human brain? *J Label Comp Radiopharm* 1991;30:293–294.

34. Dedek J, Baumes R, Tien-Duc N, Gomeni R, Korf J. Turnover of free and conjugated (sulphonyloxy)dihydroxyphenylacetic acid and homovanillic acid in rat striatum. *J Neurochem* 1979;33:687–695.

35. O'Neil JP, VanBrocklin HF. Development of a semi-remote system for the routine preparation of [18F]6-fluoro-L-meta-tyrosine to study striatal lesions and therapeutic implants in primates [Abstract]. *J Labelled Comp Radiopharm* 1995;37:655–657.

36. Nahmias C, Wahl L, Chirakal R, Firnau G, Garnett ES. A probe for intracerebral aromatic amino acid decarboxylase activity: distribution and kinetics of [18F]6-fluoro-L-m-tyrosine in the human brain. *Movement Disorders* 1995;10:298–304.

[18F]fluoroDOPA studies correlate with dopamine cell counts and levels. *Ann Neurol* 1993;34:324–330.

Three-Dimensional Imaging Characteristics of the HEAD PENN-PET Scanner

Joel S. Karp, Richard Freifelder, Michael J. Geagan, Gerd Muehllehner, Paul E. Kinahan, Robert M. Lewitt and Lingxiong Shao

Department of Radiology, University of Pennsylvania; UGM Medical Systems, Philadelphia, Pennsylvania

A volume-imaging PET scanner, without interplane septa, for brain imaging has been designed and built to achieve high performance, specifically in spatial resolution and sensitivity. The scanner is unique in its use of a single annular crystal of NaI(Tl), which allows a field of view (FOV) of 25.6 cm in both the transverse and axial directions. Data are reconstructed into an image matrix of 128^3 with $(2\ mm)^3$ voxels, using three-dimensional image reconstruction algorithms. **Methods:** Point-source measurements are performed to determine spatial resolution over the scanner FOV, and cylindrical phantom distributions are used to determine the sensitivity, scatter fraction and counting rate performance of the system. A three-dimensional brain phantom and ^{18}F-FDG patient studies are used to evaluate image quality with three-dimensional reconstruction algorithms. **Results:** The system spatial resolution is measured to be 3.5 mm in both the transverse and axial directions, in the center of the FOV. The true sensitivity, using the standard NEMA phantom (6 liter), is 660 kcps/μCi/ml, after subtracting a scatter fraction of 34%. Due to deadtime effects, we measure a peak true counting rate, after scatter and randoms subtraction, of 100 kcps at 0.7 mCi for a smaller brain-sized (1.1 liter) phantom, and 70 kcps for a head-sized (2.5 liter) phantom at the same activity. A typical ^{18}F-FDG clinical brain study requires only 2 mCi to achieve high statistics (100 million true events) with a scan time of 30 min. **Conclusion:** The HEAD PENN-PET scanner is based on a cost-effective design using NaI(Tl) and has been shown to achieve high performance for brain studies and pediatric whole-body studies. As a full-time three-dimensional imaging scanner with a very large axial acceptance angle, high sensitivity is achieved. The system becomes counting-rate limited as the activity is increased, but we achieve high image quality with a small injected dose. This is a significant advantage for clinical imaging, particularly for pediatric patients.

Key Words: three-dimensional volume imaging; positron emission tomography scanner performance

J Nucl Med 1997; 38:636–643

PET is an imaging modality that has made major advances in recent years. The spatial resolution is improved through better

detector design, and the sensitivity is improved with three-dimensional imaging and through an increase in the axial field of view. These improvements, however, have generally been accompanied by an increase in cost of the instrument. While the interest in PET continues to grow and the applications broaden, it is important that the cost of the technology does not outpace its clinical utility. Our major objectives in designing a new PET scanner were to achieve high isotropic spatial resolution and sensitivity for clinical brain studies in a cost-effective design. Design criteria were chosen to optimize these measures of performance, while tradeoffs in other areas were made.

Three basic choices were made in the design of the HEAD PENN-PET scanner:

1. Use NaI(Tl) as the detector material.
2. Focus our efforts on a small diameter system.
3. Image exclusively in three dimensions without septa.

The decision to use NaI(Tl) is largely based on the high light output of the scintillator. Anger-type position-sensitive NaI(Tl) detectors, using large photomultiplier tubes (PMTs), offer a cost-effective method of gamma-ray detection in nuclear medicine, and have been applied to 511-keV imaging since 1963 (*1*). Our group has designed several whole-body NaI(Tl) PET scanners (*2–4*), all based on hexagonal rings of six position-sensitive NaI(Tl) detectors, and most recently these same principles have been applied to a dual-detector SPECT/PET system (*5*). For this application to a dedicated brain-imaging scanner, we use a single annular crystal. For brain imaging, spatial resolution is often the most important consideration, particularly with positron-emitting isotopes with a short annihilation range, such as ^{18}F and ^{11}C. The single continuous detector leads to uniformly high spatial resolution, with fine spatial sampling, over the active area of the crystal, thus, high resolution in all three dimensions in the reconstructed images. A single continuous detector also avoids the need for scanner motion or compensation for missing data that result from having gaps between each pair of adjacent detectors used in the whole-body PENN-PET scanners (*3*).

A drawback with a continuous detector of NaI(Tl), which has

a relatively long scintillation pulse decay time ($\tau = 240$ ns), is the problem of overlapping events, or pulse pile-up, which can cause deadtime and loss of performance at high activity levels. We address this problem by reducing both temporal overlap and spatial overlap of events. The temporal overlap is reduced with pulse-clipping and short pulse integration, and the spatial overlap is reduced with a local centroid positioning algorithm which restricts the number of signals used to process an event (6).

The decision to build a small-diameter system was based on optimizing performance for brain imaging, although a small diameter is also well-suited to whole-body pediatric imaging and animal research studies. There are several advantages of using a small-diameter system for brain imaging. The first is that the spatial resolution is best in a small-diameter system, since the effect of the noncolinearity of the two annihilation photons is minimized. Second, a system with a small diameter has higher sensitivity for true coincidences for a given activity, particularly for the localized activity distributions inherent to brain imaging. While the higher sensitivity is offset somewhat by the increased acceptance of scattered radiation, the good energy resolution of NaI(Tl) helps minimize this problem. A third advantage of a small-diameter system is that it is less costly and requires fewer PMTs. Using 2-in photomultiplier tubes (PMTs), only 180 PMTs and subsequent processing channels are required. Actually, we take advantage of this cost-advantage by increasing the axial extent of the scanner at the same time we decrease the diameter. The inner diameter is 42 cm and the axial length of the crystal is 30 cm. We image a transverse field of view (FOV) of 25.6 cm, and an axial FOV is 25.6 cm, which is the largest axial FOV currently used in PET systems. Although a brain is typically 10–12 cm in axial length, the large axial FOV without septa results in a dramatic increase in the sensitivity in the central region of the FOV, where the brain is positioned.

A disadvantage of a small-diameter brain system such as ours, particularly a three-dimensional imaging system, is the lower counting rate performance compared to a large-diameter system, due to the effect of deadtime and randoms (7). Thus, this geometry is most appropriate for studies with longer-lived positron-emitting isotopes, including ^{18}F and ^{11}C, which are commonly used for metabolic and neuro-receptor imaging studies. It will not offer optimal performance for ^{15}O-water studies, which often require bolus injections with high initial activity.

The decision to continue to image exclusively in three dimensions without septa is based on previous success with the PENN-PET scanners (2–4) and that of other investigators imaging in three dimensions (8). Three-dimensional imaging has become more prevalant recently, as issues with image reconstruction and data quantitation are more effectively handled. Nearly all recent systems for both research and clinical purposes are built either without septa or with the option of retracting the septa for both two-dimensional and three-dimensional imaging (9,10). However, a significant difference between the brain-imaging scanner described here and other three-dimensional imaging scanners is the increased range of out-of-plane angles that are accepted. For this brain-imaging system, the maximum axial acceptance angle, α, defined as the co-polar angle from the center of the scanner, is 28°, whereas other scanners with three-dimensional imaging capability (11–13), generally have a larger diameter and smaller axial extent, with $\alpha \sim 10$–16°. The large acceptance angle affects several aspects of system performance, including spatial resolution, scattered radiation, counting rate performance and the accuracy
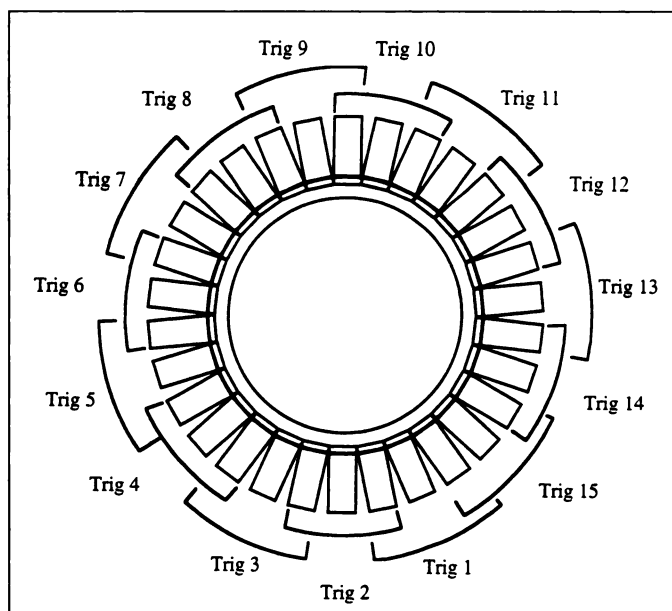
FIGURE 1. Schematic of detector shows 30 columns of PMTs, each column with six rows, using 15 overlapping triggers.

of the three-dimensional reconstruction algorithm. These measures of performance have been carefully evaluated, and results are reported in this paper.

The image reconstruction algorithm, in particular, has been studied as a function of α (14–15). We have found the three-dimensional reprojection (3DRP) algorithm (16) to perform well, in terms of accuracy and signal-to-noise ratio for large α, using both simulated and experimental data (14–15). However, since it requires special hardware to accelerate its otherwise long reconstruction time, other algorithms which reduce the data size and/or increase the speed of reconstruction, are also of interest. In particular, the multislice rebinning algorithm (MSRB) (17) and the Fourier rebinning algorithm (FORE) (18) are promising. We have prior experience with the MSRB algorithm, which is considerably faster than the 3DRP algorithm and, because of the more compact size of the sinogram data, it is more suitable for multiframe dynamic studies. In this article, where we wish to retain a focus on the intrinsic capabilities of this scanner, we illustrate reconstructed image quality with the 3DRP algorithm, since this algorithm provides the highest signal-to-noise ratio and best image quality. However, appropriate use of the MSRB, FORE or other approximate reconstruction algorithms will be determined as we perform further studies with the HEAD PENN-PET system.

DESIGN

The basic design of the HEAD PENN-PET scanner has been previously described (19). The electronic processing is based on earlier work (20) with the addition of local coincidence triggering (21), which is essential for a continuous detector. Here, we briefly summarize the design with an emphasis on those areas that are significant for the results reported in this article.

Detector, Electronics and Position Processing

The NaI(Tl) annular crystal has an inner diameter of 42 cm, is 30 cm long and 1.9 cm thick. A segmented light guide, with 30 facets, is bonded to the back surface, to which 30 columns by six rows of 2-in square PMTs are coupled. In order to use a single crystal for coincidence detection, it is important that the light from each event does not spread too far. Due to the geometrical and reflective properties of the crystal (and light guide) most of the light from an event is measured by small
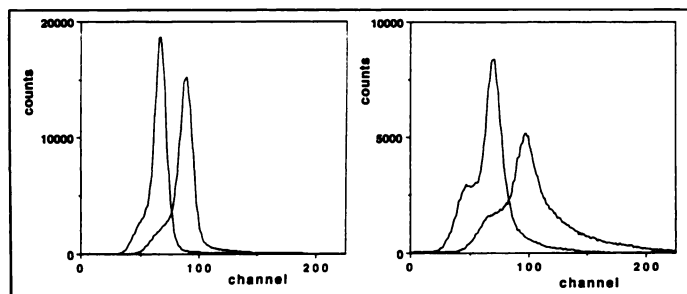
FIGURE 2. Local and global energy spectra at low (left) and high (right) counting rates.

groups of the nearest PMTs. Thus, we can identify photopeak events by summing three columns of PMTs into constant fraction discriminators, forming a total of 15 overlapping triggers, as illustrated in Figure 1. The timing triggers have the lower level threshold set at 350 keV, although subsequent software energy gates define a photopeak window from 450–580 keV before rebinning. Coincidences are determined (with a 10-ns timing window) between valid pairs of triggers, which determine the transverse field of view of 25.6 cm. While all of the PMTs are continuously digitized, after pulse clipping, the triggers instruct the electronics to begin integration (for 200 ns) and processing for two zones of PMTs corresponding to the coincident trigger circuits.

Within the larger zone of PMTs, a smaller cluster is determined for calculation of a local energy and local centroid position. The use of a small cluster yields a stable energy and position at high counting rates, although the effect of pileup of simultaneous events eventually becomes noticeable. As an illustration, Figure 2 compares the local energy spectrum using a cluster of nine PMTs, to a global energy spectrum using a cluster of 30 PMTs. The data were acquired using a uniformly filled phantom with less than 0.1 mCi for the low counting rate spectra, and about 0.8 mCi for the high counting rate spectra, where the total detector singles rate is 7.5 Mcps. At this rate, the local energy spectrum is much less degraded than the global energy spectrum. From the low counting-rate data, one observes that the photopeak of the local energy spectrum is about 70% that of the global energy spectrum, representing the fraction of scintillation light that is measured by the small cluster. The loss of light has a small effect on the measured energy resolution (FWHM), since the local energy resolution is 11% compared to 10% for the global energy. In addition, we achieve a measured detector point spread function, for 511-keV photons, of 4.5 mm (FWHM), in both directions (*19*). Note that these measurements include pulse clipping and 200-ns integration, which means that only about 60% of the scintillation light emitted in NaI(Tl) is used.

A consequence of using a small PMT cluster is that the measured position is discontinuous between adjacent PMTs. To ensure that the calcuated position changes continuously, and linearly, across the entire crystal a method of spatial distortion correction is required (*22*). A correction table is calculated after the distortion measurement, then, during data acquisition, the measured coordinates of each event are used as an address to the distortion correction table, and a real position is calculated. The circumferential position (x-coordinate) is sorted into 0.4-mm bins while the axial position (z-coordinate) is sorted into to 1.0-mm bins.

### Data Processing and Image Reconstruction

After energy gating, the data can be rebinned in real time into sinograms for SSRB or MSRB reconstruction or projection matrices for FORE or 3DRP reconstruction. For sinogram rebinning, the x- and z-coordinates on the detector surface are converted into standard sinogram coordinates (r, ϕ) and a range of slice numbers, depending on the co-polar (out-of-plane) angle of the coincident line-of-response. The axial deblurring for MSRB occurs off-line during image reconstruction. The sinogram data are stored as 256 rays by 192 angles in 128 slices, for a total of 12 Mbytes. To achieve a transverse FOV of 25.6 cm and axial FOV of 25.6 cm, the data are sorted into 1-mm bins in the transverse direction and 2-mm bins in the axial direction. It is possible to sample more finely in both directions, but for a more limited FOV. Alternately, doubling the bin size in the transverse direction, the sinograms can be *reduced* by a factor of four (128 rays by 96 angles), for a total of only 3 Mbytes for 128 slices. The smaller sinograms save space and decrease the transfer time to the host computer, which is important for dynamic acquisitions.

For flexibility in data processing, data are written in list-mode and rebinning is performed off-line. The list-mode data are stored either without energy information or with energy from both detectors, thus allowing final gating to be determined after data collection. Storing the data without energy information requires 6 bytes per event and 12 bytes per event with energy information. For the 3DRP reconstructions presented in this article, the list-mode data are rebinned into four-dimensional projection matrices (x', y', ϕ, θ) that are 128 × 128 × 96 × 15, for a total of 48 Mbytes, where each projection bin is 2 bytes deep. The spatial sampling, 2 mm, is comparable to the spatial sampling of the *reduced* sinogram size (128 × 96) used for MSRB. The projection data are then reconstructed to a 128^3 image matrix, with uniform $(2 \text{ mm})^3$ sampling in transverse and axial directions.

After rebinning, the data are normalized for uniform efficiency. One important correction involves the sampling pattern that results from histogramming the data from the very fine detector coordinate system to the coarser sinograms (for SSRB or MSRB) (*2*) or projection data (for 3DRP) (*15*). A second correction involves the intrinsic detector nonuniformities. Our correction for the detector nonuniformities follows the method of Casey et al. (*23*) for both the sinograms and modified for application to projections. For the circular geometry of the HEAD PENN-PET scanner we perform normalization using a cylindrical phantom with a uniform distribution, with appropriate corrections for geometry and attenuation of the phantom.

In addition, we have implemented quantitative correction methods for scatter, attenuation and randoms. For the MSRB algorithm, the correction methods are applied to the sinogram data and follow those developed for the SSRB algorithm (*3*). Since we anticipated the increased importance of scatter correction in a volume-imaging scanner with a large axial acceptance angle, we have re-evaluated the tail-fitting method applied to both sinogram data (*3*) and projection data (*15*), and compared it to alternative methods, such as two-dimensional deconvolution (*24*) and energy-based scatter correction (*25,26*). While the deconvolution and energy-based methods have advantages under certain circumstances, for the data presented here we used the tail-fitting method for the following reasons. For relatively uniform distributions, which include metabolic and flow studies of the brain, the tail-based method provides a fair estimate of scatter and can estimate the sum of scatter and randoms over a wide range of counting rates. This method also takes into consideration scatter from outside the field of view, which deconvolution correction methods do not. In our implementation, a parabolic fitting is used, although other smoothly
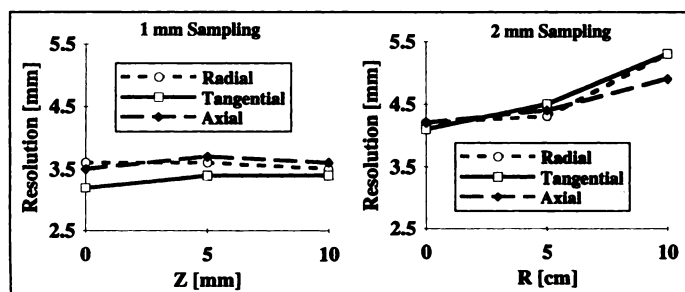
FIGURE 3. Radial (short dash), tangential (solid) and axial (long dash) resolution (FWHM) as a function of axial position (left), with 1-mm spatial sampling, and radius (right), with 2-mm spatial sampling.

varying functions can also be used, such as a Gaussian function *(27)*.

The method of attenuation correction for the brain studies performed to date is provided by calculating the chord length through the head for each projection, based on the outline of ellipses fit to the contour of the head. This is performed in two dimensions, slice by slice, with sinogram data, and in three dimensions, using a three-dimensional surface created from the stack of ellipses, with projection data. Since an ellipse does not always provide a good estimate of skull contour, particularly near the base of the brain, we have investigated the application of an automated technique for fitting the skull surface from projection data, in order to determine the attenuation length for each projection *(28)*. While this method may be an improvement over ellipse fitting, it will still not properly compensate for the nasal passages in the head or for the lungs in whole-body pediatric studies. Therefore, we will next install a transmission source for attenuation correction, and implement the single-photon method using [137]Cs *(29)*, as currently done for the whole-body PENN-PET scanner.

After data correction and two-dimensional filtered backprojection with a Hanning filter, MSRB data are deblurred axially, using a singular-value decomposition *(17)*. Subsequent Wiener filtering *(30,31)* is performed, based on measurements of the system modulation transfer function. This results in a noticeable improvement in image quality, in terms of both count recovery and contrast improvement in the images, with increased signal-to-noise ratio. With the 3DRP reconstruction, a Hanning filter is first applied in both the transverse and axial directions, followed by the method of Wiener postfiltering.

SYSTEM PERFORMANCE MEASUREMENTS

Since the preliminary performance measurements reported in Freifelder et al. *(19)*, the detector assembly has been installed in a permanent gantry, suitable for patient studies. We have also studied the system performance in more detail in order to characterize the practical operation of the system for patient studies. The measurements follow the style of the SNM/NEMA standard tests *(32,33)*, but a smaller cylindrical phantom is used for scatter and counting rate measurements. We used both a brain-sized phantom, 12-cm diameter by 10-cm cylinder (1.1 liter) and a head-sized phantom, 18-cm diameter by 10-cm cylinder (2.5 liter). In contrast, the SNM/NEMA standard phantom is 20-cm diameter by 19-cm long, and 6 liters in volume, which is a good compromise for scanners that are capable of both brain and whole-body imaging, but for a dedicated brain scanner, the NEMA phantom *overestimates scatter* and underestimates counting rate capability. Actually, the NEMA phantom was not designed to be used in a scanner longer than 16 cm so that these measurements cannot be

directly compared between a scanner with a large axial FOV (>16 cm) and one with a small FOV.

Spatial Resolution

Spatial resolution has been measured over the transverse and axial FOV, out to radial and axial distances of ± 10 cm from the center, using a small ^{18}F source (0.5 mm³). The intrinsic system resolution, in tangential, radial and axial directions, has been measured by rebinning the data with the single-slice rebinning algorithm *(3)* with a restricted axial acceptance angle (±2°), and the MSRB and 3DRP algorithms with the axial acceptance angle unrestricted ($\alpha = 28°$). Ramp-filtered backprojection was used in all three cases. The SSRB and MSRB algorithms allow both 1-mm and 2-mm spatial sampling, whereas the 3DRP uses only 2-mm sampling. We measure 3.5-mm (FWHM) transverse and axial resolution in the center with 1-mm sampling (with SSRB and MSRB algorithms) and 4.0-mm with 2-mm sampling (with SSRB, MSRB and 3DRP algorithms). For patient imaging, 2-mm sampling is used to achieve both a 256-mm transverse and axial FOV. Figure 3 shows that the resolution is approximately uniform in all three directions and degrades slowly as the radial distance increases. We have shown that the MSRB and 3DRP algorithms, using all oblique lines of response (with $\alpha = 28°$) are of comparable accuracy, though the measured spatial resolution, with either algorithm, is partly limited by spatial sampling.

The effect of high counting rates on resolution was measured with a high intensity source. With a total detector singles counting rate of 7.5 Mcps above the trigger threshold, the spatial resolution degrades a little more than 10% compared to the low counting rate result. Thus, in the center of the scanner, the FWHM increases from 4.0–4.5 mm (2-mm sampling) as the counting rate increases to 7.5 Mcps, while the FWTM increases from 9.7–11.4 mm at the same rate. Although this indicates that there is some degradation in detector performance at very high counting rates, due to pulse pile-up, the temporal and spatial processing of the signals help minimize the effect at typical counting rates. For example, clinical ^{18}F-FDG brain studies result in a total detector singles counting rate of between 3 and 4 Mcps, so that the degradation in spatial resolution for these studies is small.

Sensitivity and Scatter

The axial sensitivity profile of a septa-less scanner, with the axial acceptance angle unrestricted, is a triangular function peaked in the center. With the standard NEMA phantom (20 cm diameter by 19 cm long), the measured true sensitivity is 660 kcps/μCi/ml, after subtracting a scatter fraction of 34%. The scatter fraction (scatter/total) was measured by the NEMA method *(33)* using a photopeak energy window of 450–570 keV. As mentioned, the NEMA measurement does not properly consider a scanner whose axial length is longer than the phantom, thus the total system sensitivity is very sensitive to the phantom length. Therefore, since comparisons with other scanners are difficult, we instead focus on a phantom closer to the size of a typical patient's head in both diameter and length so as to better understand characteristics of the scanner for patient studies. We also quote the sensitivity normalized for axial-cm. Using the head-sized 2.5-liter phantom, the true sensitivity, after subtracting a scatter fraction (measured specifically with this phantom) of 29%, is 50 kcps/μCi/ml/axial-cm at the center, or 10 kcps/μCi/ml for a 2-mm thick transaxial slice. Although the sensitivity drops off at the ends of the scanner, as it does for every volume imaging system without septa, most subjects' heads can be positioned in the central part of the field of view where the sensitivity is highest. Assuming that the brain is
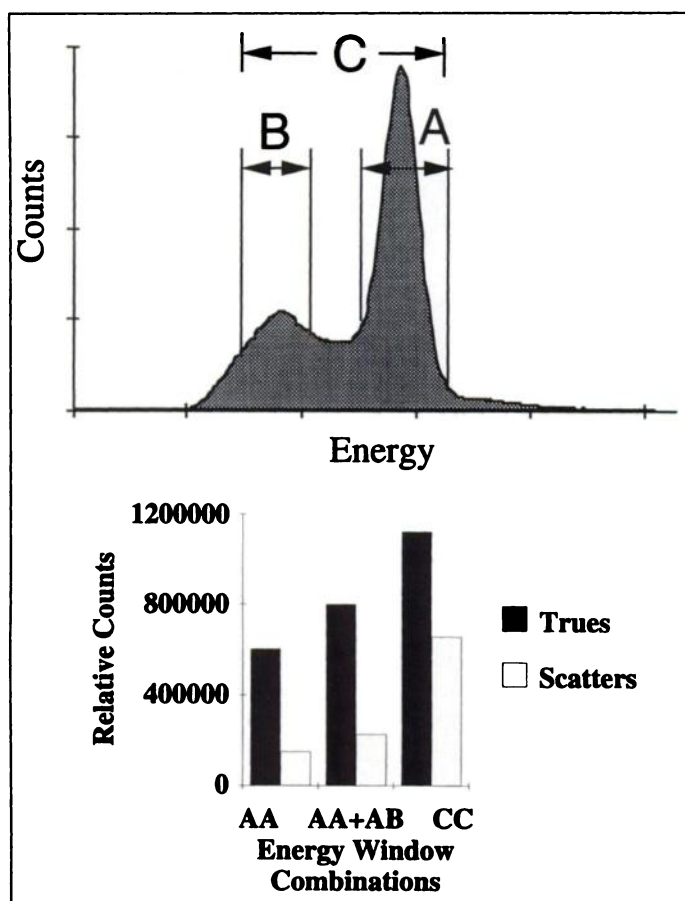
FIGURE 4. (Top) Energy spectrum (for one detector) with (A) photopeak window, (B) Compton window and (C) total window. (Bottom) Histogram of true events and scatter events measured in each of three energy window combinations of the two detectors, 1 and 2. The three combinations are: (a) AA = Photopeak-Photopeak (A1, A2); (b) AA + AB = Photopeak-Photopeak + Photopeak-Compton ((A1, A2) + (A1, B2) + (A2, B1)); and (c) CC = total (C1, C2).

centered in the scanner, the sensitivity at the edge of the brain (approximately at 6.4 cm from the center) will be about half the value in the center, or 25 kcps/μCi/ml/axial-cm. Compared to the PENN-PET 240H scanner (3), our whole-body imaging scanner (diameter = 84 cm, axial length = 12.8 cm), the sensitivity of the brain scanner is a factor of 3 higher in the center and a factor of 30 higher at an axial distance of 6.4 cm from the center.

The current imaging protocol uses a photopeak energy window for each detector, but it is also possible to set two energy windows with on-line rebinning. One use of the second energy window is to improve sensitivity for true events (34,35), using the good energy resolution of NaI(Tl). The energy region above the Compton edge, from about 340–450 keV, contains mainly scattered events (scatter within the object medium) with few true events. Directly below 340 keV, however, are scattered events as well as true events, which Compton scatter out of the crystal. We set two energy windows, a primary photopeak Window A from 450–570 keV, and a secondary Window B from 250–340 keV, excluding the events between 340–450 keV. Here we measure the sensitivity using a uniform activity distribution in the 2.5-liter phantom and estimate the scatter fraction using the tail-fitting method (3), normally applied as a scatter correction method before image reconstruction. It is worth noting that the scatter fraction measured by the NEMA method (33), which estimates scatter from the line spread function of sources in water, includes forward, small-angle

scattering. These events have a spatial distribution similar to the distribution of the true events and do not affect image quality as adversely as large-angle scattering. The tail-fitting method cannot discriminate these forward-scattered events from the true events, thus we measure a scatter fraction for the 2.5-liter phantom of only 20% using the tail-fitting method, compared to 29% using the NEMA measurement. For this comparison of single- versus dual-energy windows, the relative differences are more relevant than the absolute values, thus we quote only scatter fraction values based on tail-fitting.

Figure 4 shows the relative sensitivity and scatter measured using only the single "photopeak-photopeak" window for both detectors (A1, A2) and using the dual windows by adding the "photopeak-photopeak" window and the "photopeak-Compton" windows, in other words (A1, A2) + (A1, B2) + (A2, B1). The inclusion of (B1, B2) is not significant because there are few counts in this window. By using the dual windows, we increase the true sensitivity by about 32% while increasing the scatter fraction only from 20% to 22%. As a comparison, we also tested a wide single Window C from 250–570 keV using this single total window (C1, C2), the true sensitivity increases by 86%, but the scatter fraction significantly increases to 37%. Therefore, using the dual "photopeak-photopeak" and "photopeak-Compton" windows may be advantageous for patient studies, since we can achieve a higher sensitivity without significantly increasing the scatter fraction. This has not been rigorously validated using either phantom or patient studies. However, isolated studies in which the data have been collected in list mode, and which have been reconstructed using different energy window combinations, seem to confirm that there is an advantage in using the dual-energy windows.

Counting Rate Capability

Since we wish to characterize performance for patient brain studies, primarily ^{18}F-FDG studies, we performed counting rate measurements using the NEMA protocol, but using the smaller 1.1-liter and 2.5-liter phantoms, as shown in Figure 5. At about 0.7 mCi activity, the total detector singles counting rate is 7 Mcps, and the coincident counting rate is about 600 kcps for the 1.1-liter phantom and 500 Mcps for the 2.5-liter phantom. After energy gating, but without processing deadtime, the coincident counting rate of valid events (which fall within the predetermined transverse field of view of 25.6 cm) reaches 240 kcps for the small phantom and 200 kcps for the larger phantom, since the energy gate accepts only 40% of coincident events at this rate. As comparison, at low counting rates, where pulse pile-up is negligible, the energy gate accepts about 60% of coincident events, with the hardware trigger set to 350 keV. With the current hardware, the processing of coincident events saturate at 500 kcps, though upgraded hardware results in an increased processing rate up to 700 kcps. At 0.7 mCi, the processing deadtime, together with the energy gating requirement, result in a final event rate of 150 kcps for the 1.1-liter phantom and 135 kcps for the 2.5-liter phantom. After scatter and randoms subtraction, the true event rate is 100 kcps for the small phantom and 70 kcps for the large phantom. The corresponding randoms fractions (randoms/trues) are 25% and 55%. Thus, considering the peak true counting rate, the randoms fraction and the deadtime, 0.7 mCi represents a reasonable limit of activity in the system. In addition, spatial resolution was shown to suffer only a small degradation at detector singles counting rates corresponding to this activity (about 7 Mcps).
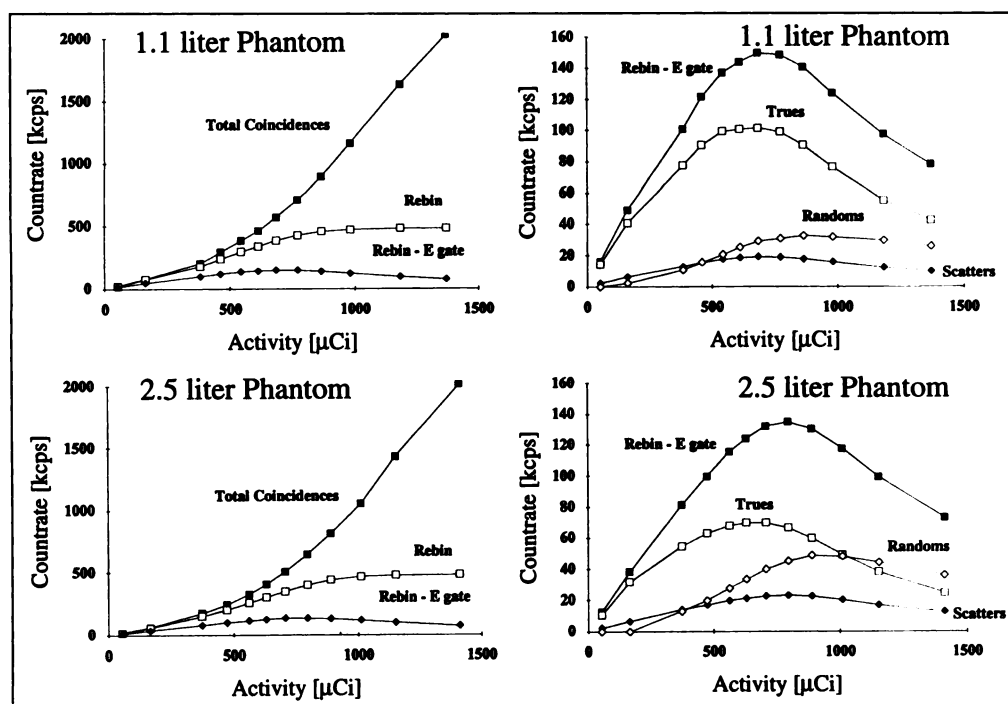
FIGURE 5. System counting rates with the 1.1- and 2.5-liter phantoms. The left panels show the total coincidence rate and the rebinning rate with and without energy gating. The right panels are the total rebinning rate with energy gating and the contribution of true, scatter and random events.

IMAGING RESULTS

The three-dimensional brain phantom (Hoffman phantom) has become a standard for demonstrating image quality. We imaged this phantom with ^{18}F and reconstructed the data with the 3DRP algorithm (Fig. 6), using the standard processing parameters described in Section 2.2. The only difference between this study and the standard patient protocol is a longer imaging time so as to acquire a total of 200 million counts.

An ^{18}F-FDG study on an adult volunteer is shown in Figure 7. The injected dose was only 30 μCi/kg, for a total of 1.9 mCi. For these studies, the data were collected in list mode which limits the acquisition counting rate (due to disk transfer time) to about 50 kcps. The volunteer was scanned for about 1 hr, for a total of 150 million counts. Our normal scan time for clinical ^{18}F-FDG studies is 30–40 min, which typically yields 100

million counts. The injected dose for patient studies is one-third the dose used for studies with the PENN-PET 240H. On the brain scanner the smaller dose yields an average true counting rate of 50–60 kcps, compared to a true counting rate of about 25–30 kcps with the PENN-PET 240H (36), using a larger injected dose (e.g., 8 mCi for a 70-kg adult).

One other example is presented in Figure 8 to illustrate the benefit of using the HEAD PENN-PET scanner for pediatric imaging. The study is of a 5-mo-old baby, where only 0.5 mCi ^{18}F-FDG was injected. The cardiac, whole-body study was 10 min in duration, followed by a 30-min brain study. The whole-body study shown in Figure 8 does not have attenuation correction.

DISCUSSION

We have built and evaluated a high-performance PET scanner with a very large axial extent, without septa, to achieve high
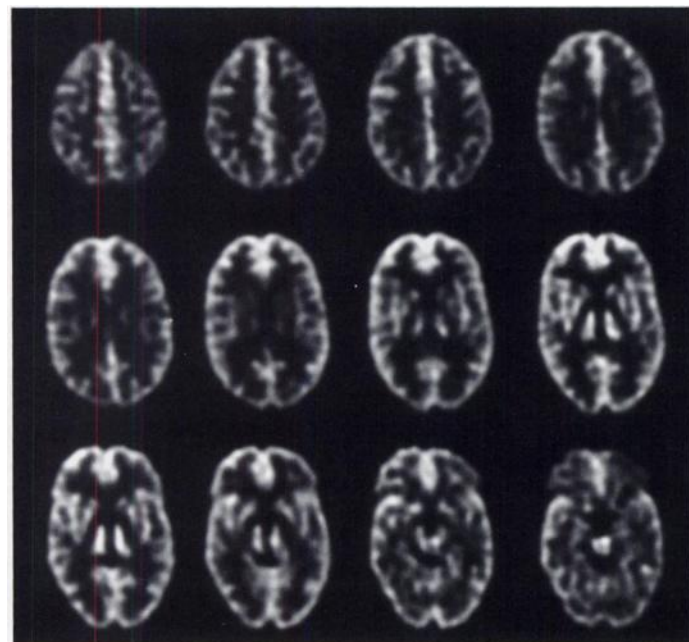
FIGURE 6. Representative transverse images (each 2-mm thick) of the three-dimensional brain phantom imaged with [18]F. The 3DRP algorithm was used for image reconstruction.
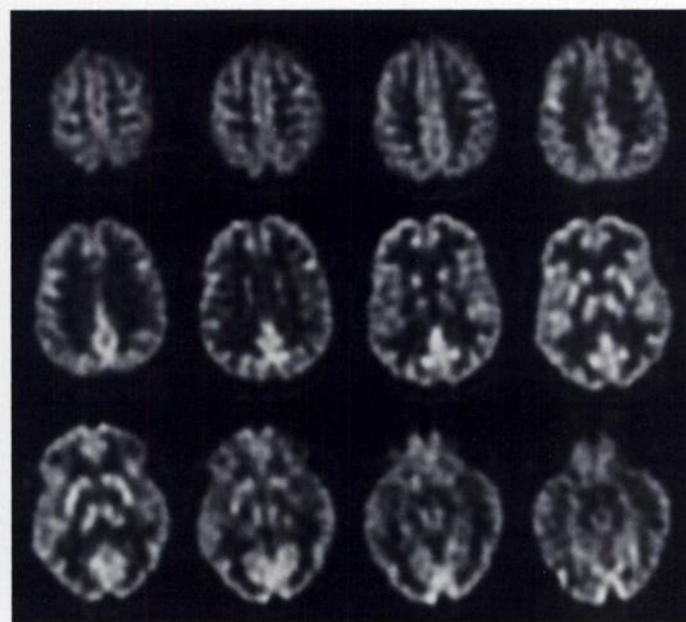
FIGURE 7. Representative transverse images (each 2-mm thick) of ^{18}F-FDG brain study. The 3DRP algorithm was used for image reconstruction.
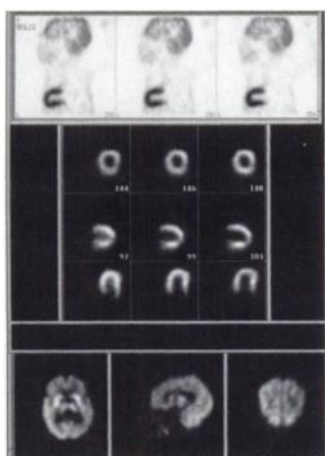
FIGURE 8. Fluorine-18-FDG study of 5-mo-old baby. The baby was repositioned between the whole-body/cardiac study (top/middle) and the brain study (bottom). Since the baby was lying on its side, the cardiac and brain images were resliced after reconstruction to display short axis and long axis views for the heart, and transverse, sagittal and coronal views for the brain. All images are 2-mm thick. Note the reversal of the color scale between the top and middle images.

sensitivity with three-dimensional imaging techniques. The scanner encompasses an imaging volume of 256 mm diameter in the transverse direction by 256 mm long in the axial direction. The data are reconstructed into a 128^3 matrix, with (2 mm)^3 cubic voxels, thus the images can viewed as 128 slices in the transaxial, sagittal or coronal planes. Using a position-sensitive NaI(Tl) detector consisting of a single annular crystal, very fine spatial sampling can be used to achieve very high spatial resolution of 3.5 mm (FWHM) in both the transverse and axial directions. The design, using a single crystal and only 180 photomultipliers, is very cost effective, given the large axial extent. Although NaI(Tl) has lower stopping power than BGO for 511-keV gamma rays, the large geometrical solid angle of the scanner leads to a high sensitivity for true coincident events. An important attribute of NaI(Tl) is the good energy and timing resolution, which helps to minimize the scatter fraction and randoms fraction in a septa-less system. Even with pulse-clipping and short integration, we achieve 10%–11% energy resolution. In addition, these signal processing techniques, together with the method of position processing, yield high spatial resolution and overall performance at a total detector singles rate of at least 7.5 Mcps.

We also have demonstrated that the consequences of imaging with a very large axial acceptance angle ($\alpha = 28°$). First, the scatter and randoms fractions are moderated using narrow photopeak energy gates. Second, the intrinsic spatial resolution is preserved using an accurate three-dimensional reconstruction algorithm, including the MSRB and the three-dimensional reprojection algorithms. For clinical brain studies, the multislice rebinning algorithm (MSRB) performs well, but the images are noticeably noisier than the reprojection algorithm (3DRP). The drawback of using the 3DRP algorithm is the large data storage and reconstruction time required, but these issues can be partly overcome without additional computing power by reducing the size of the projection dataset. We are currently evaluating the performance of the algorithm with a larger bin size of the co-polar angle, thereby reducing the number of out-of-plane angles. For example, for online acquisition, we reduce the data size by a factor of two by increasing the out-of-plane bin width $\Delta\theta$ from 3.75° to 7.5°. This is still more accurate than our utilization of single-slice rebinning with the PENN-PET 240H, where the out-of-plane angles are effectively reduced into a single value corresponding to a much larger $\Delta\theta$ of 13° (alternately expressed as the maximum axial acceptance angle $\alpha = 6.5°$). Therefore, we expect to achieve very good results with the increased bin width $\Delta\theta$ with the three-dimensional rebinning, and the three-dimensional reconstruction is significantly faster, as well.

The HEAD PENN-PET scanner has been shown to be suitable for brain imaging of adults and children as well as pediatric whole-body imaging. Compared to most other systems, including the previous PENN-PET 240H design with a smaller axial acceptance angle, the dose delivered to the patient is significantly reduced, which is an advantage, particularly for pediatric imaging. For adults, we inject 30 μCi/kg. We have also imaged extremities, specifically the foot. In addition, small rats have been imaged, using ^{18}F-FDG, and expect further use to include radiochemistry ligand research and gene therapy research.

While the HEAD PENN-PET scanner has very high sensitivity, the system becomes counting-rate limited above an activity of 0.7 mCi in the field of view. This does not pose a problem for clinical ^{18}F-FDG studies, although increased counting rate capability would be beneficial for wider applicability with short-lived isotopes.

CONCLUSION

We have described a new PET scanner based on a single continuous NaI(Tl) detector, in a design suitable for brain imaging as well as pediatric whole-body imaging. The spatial resolution is 3.5 mm, uniformly in all directions, and the sensitivity is high, as imaging is performed exclusively in three dimensions. The axial FOV is 25.6 cm and data are reconstructed into 128 transaxial slices with 2-mm spacing. We achieve good statistics and image quality for clinical ^{18}F-FDG studies using a low injected dose of 2–4 mCi for adults. Lower doses are used for children. The scanner is low cost and reliable, making it suitable for both a clinical and research environment, but with high performance that is required for many PET applications.

ACKNOWLEDGMENTS

REFERENCES

1. Anger HO. Gamma-ray and positron scintillation camera. *Nucleonics* 1963;21:10–56.
2. Muehllehner G, Karp JS. A positron camera using position-sensitive detectors: PENN-PET. *J Nucl Med* 1986;27:90–98.
3. Karp JS, Muehllehner G, Mankoff DA, et al. Continuous-slice PENN-PET: a positron tomograph with volume imaging capability. *J Nucl Med* 1990;31:617–627.
4. Karp JS, Kinahan PE, Muehllehner G, Countryman P. Effect of increased axial field of view on the performance of a volume PET scanner. *IEEE Trans Med Imaging* 1993;12:299–306.
5. Muehllehner G, Geagan M, Countryman P, Nelleman P. SPECT scanner with PET coincidence capability. *J Nucl Med* 1995;35:70.
6. Mankoff DA, Muehllehner G, Karp JS. The high countrate performance of a two-dimensionally position-sensitive detector for positron emission tomography. *Phys Med Biol* 1989;34:437–456.
7. Stearns CW, Cherry SR, Thompson CJ. NECR analysis of 3D brain PET scanner designs. *IEEE Trans Nucl Sci* 1995;42:1075–1079.
8. Diffey BL, ed. Fully 3D image reconstruction. *Phys Med Biol* 1994;39: entire issue.
9. Townend DW, Spinks TJ, Jones T, Geissbuhler A, Defrise M, Gilardi MC, Heather J. Three-dimensional reconstruction of PET data from a multi-ring camera. *IEEE Trans Nucl Sci* 1989;36:1056–1065.

10. Cherry S, Dahlbohm M, Hoffman EJ. Three-dimensional PET using a conventional multi-slice tomograph without septa. *J Comput Assist Tomogr* 1991;15:6455–6468.
11. Townsend D, Byars L, Defrise M, Geissbuhler A, Nutt R. Rotating positron tomographs revisited. *Phy Med Biol* 1994;39:401–410.
12. Wienhard K, Eriksson L, Grootoonk S, Casey M, Pietryzk U, Heiss W-D. Performance evaluation of the positron scanner ECAT EXACT. *J Comput Assist Tomogr* 1992;16:804–813.
13. De Grado T, Turkington T, Williams J, Stearns C, Hoffman J, Coleman R. Performance characteristics of a whole-body PET scanner. *J Nucl Med* 1994;35:1398–1406.
14. Kinahan PE, Karp JS. Figures of merit for the performance of a volume imaging PET scanner. *Phys Med Biol* 1994;39:631–642.
15. Kinahan PE. Image reconstruction algorithms for volume-imaging PET scanners [PhD thesis]. University of Pennsylvania; Philadelphia: 1994.
16. Kinahan PE, Rogers JG. Analytic 3D image reconstruction using all detected events. *IEEE Trans Nucl Sci* 1989;36:964–968.
17. Lewitt RM, Muehllehner G, Karp JS. Three-dimensional image reconstruction for PET by multi-slice rebinning and axial image filtering. *Phys Med Biol* 1994;39:321–339.
18. Defrise M. A factorization method for the 3D x-ray transform. *Inverse Problems* 1995;11:983–994.
19. Freifelder R, Karp JS, Geagan M, Muehllehner G. Design and performance of the HEAD PENN-PET scanner. *IEEE Trans Nucl Sci* 1994;41:1436–1440.
20. Karp JS, Muehllehner G, Beerbohm D, Mankoff D. Event localization in a continuous scintillation detector using digital processing. *IEEE Tran Nucl Sci* 1986;33:550–555.
21. Mankoff DA, Muehllehner G, Miles GE. A local coincidence triggering system for PET tomographs composed of large-area position-sensitive detectors. *IEEE TNS* 1990;37:730–736.
22. Geagan MJ, Chase BB, Muehllehner G. Correction of distortions in a discontinuous image. *Nucl Instr Meth A* 1994;353:379–383.
23. Casey ME, Hoffman EJ. Quantitation in positron emission tomography: 7. A technique to reduce noise in accidental coincidence measurements and coincidence efficiency calibration. *J Comput Assist Tomogr* 1986;10:845–850.
24. Shao L, Karp JS. Cross plane scattering correction-point source deconvolution in PET. *IEEE Trans Med Imaging* 1991;10:234–239.
25. Grootoonk S, Spinks TJ, Jones T, Michel C, Bol A. Correction for scatter using a dual energy window technique with a tomograph operating without septa. *IEEE Medical Imaging* 1991;10:1569–1573.
26. Shao L, Freifelder R, Karp JS. Triple energy window correction technique in PET. *IEEE Trans Med Imaging* 1994;13:641–648.
27. Stearns CW. Scatter correction method for 3D PET using 2D fitted Gaussian functions. *J Nucl Med* 1995;36:105P.
28. Yan MXH, Karp JS. A fully automated algorithm for estimating attenuation length in 3D from projection data. *Conference Record of the 1995 IEEE Medical Imaging* 1995;3:1407–1410.
29. Karp JS, Muehllehner G, Qu He, Yan XH. Singles transmission in volume-imaging PET with a 137Cs source. *Phys Med Biol* 1995;40:929–944.
30. Shao L, Karp JS, Countryman P. Practical considerations of the Wiener filtering technique on projection data for PET. *IEEE Trans Nucl Sci* 1994;41:1560–1565.
31. Shao L, Lewitt RM, Karp JS. Combination of Wiener filtering and singular value decomposition filtering for volume imaging PET. *IEEE Trans Nucl Sci* 1995;42:1228–1234.
32. Karp JS, Daube-Witherspoon ME, Hoffman EJ, et al. Performance standards in positron emission tomography. *J Nucl Med* 1991;32:2342–2350.
33. Performance measurements of positron emission tomographs. *NEMA Standards Publication NU 2–1994*. Washington, DC: NEMA; 1994.
34. Muehllehner G, Buchin MP, Dudek JH. Performance characteristics of a positron imaging camera. *IEEE Trans Nucl Sci* 1976;23:528–537.
35. Thompson CJ, Picard Y. Two new strategies to increase the signal-to-noise ratio in positron volume imaging. *IEEE Trans Nucl Sci* 1993;40:956–961.
36. Smith RJ, Karp JS, Muehllehner G. The countrate performance of the volume imaging PENN-PET scanner. *IEEE Trans Med Imag* 1994;13:610–618.

FIRST IMPRESSIONS
Gallium and Hepatic Scintigraphy
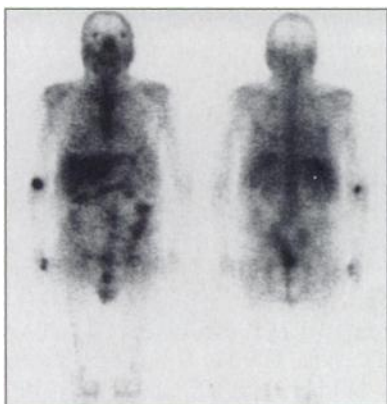
Figure 1.
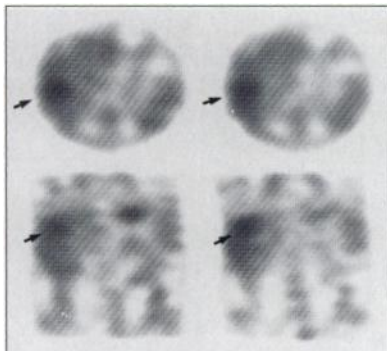
PURPOSE
A 55-yr-old man with large-cell non-Hodgkin's lymphoma was suspected of recurrence after 3 yr of continuous clinical remission. CT showed a mass in the right lobe of the liver, but planar ⁶⁷Ga scintigraphy appeared normal (Fig. 1). However, SPECT imaging of the liver (Fig. 2) showed focal ⁶⁷Ga uptake in the right lobe (arrows) corresponding to the pathology on CT. Gallium-67 cannot be interpreted without SPECT imaging.

TRACER
Gallium-67-citrate, 8 mci

ROUTE OF ADMINISTRATION
Intravenous

TIME AFTER INJECTION
48 hours and one week

INSTRUMENTATION
Elscint Helix dual-head camera with HPC-5 medium-energy collimator

CONTRIBUTORS
Jabour Khoury and Rachel Bar-Shalom, Department of Nuclear Medicine, Rambam Medical Center, Haifa, Israel.

Figure 2.